Oxidative Coupling of Methane over Pt/Al$_2$O$_3$ at High Temperature: Multiscale Modeling of the Catalytic Monolith

Jaspreet Chawla [1], Sven Schardt [1], Sofia Angeli [1], Patrick Lott [1], Steffen Tischer [2], Lubow Maier [2], and Olaf Deutschmann [1,2,*]

[1] Institute for Chemical Technology and Polymer Chemistry (ITCP), Karlsruhe Institute of Technology (KIT), 76131 Karlsruhe, Germany; jaspreet.chawla@kit.edu (J.C.); sven.schardt@kit.edu (S.S.); sofia.angeli@kit.edu (S.A.); patrick.lott@kit.edu (P.L.)

[2] Institute of Catalysis Research and Technology (IKFT), Karlsruhe Institute of Technology (KIT), 76344 Eggenstein-Leopoldshafen, Germany; steffen.tischer@kit.edu (S.T.); lubow.maier@kit.edu (L.M.)

* Correspondence: deutschmann@kit.edu

Abstract: At high temperatures, the oxidative coupling of methane (OCM) is an attractive approach for catalytic conversion of methane into value-added chemicals. Experiments with a Pt/Al$_2$O$_3$-coated catalytic honeycomb monolith were conducted with varying CH$_4$/O$_2$ ratios, N$_2$ dilution at atmospheric pressure, and very short contact times. The reactor was modeled by a multiscale approach using a parabolic two-dimensional flow field description in the monolithic channels coupled with a heat balance of the monolithic structure, and multistep surface reaction mechanisms as well as elementary-step, gas phase reaction mechanisms. The contribution of heterogeneous and homogeneous reactions, both of which are important for the optimization of C2 products, is investigated using a combination of experimental and computational methods. The oxidation of methane, which takes place over the platinum catalyst, causes the adiabatic temperature increase required for the generation of CH$_3$ radicals in the gas phase, which are essential for the formation of C2 species. Lower CH$_4$/O$_2$ ratios result in higher C2 selectivity. However, the presence of OH radicals at high temperatures facilitates subsequent conversion of C$_2$H$_2$ at a CH$_4$/O$_2$ ratio of 1.4. Thereby, C2 species selectivity of 7% was achieved at CH$_4$/O$_2$ ratio of 1.6, with 35% N$_2$ dilution.

Keywords: oxidative coupling methane; kinetic modeling; platinum catalyst; acetylene

1. Introduction

Methane, the main component of natural gas, is burnt for heating purposes but is also an important chemical feedstock for the production of syngas by steam reforming, dry reforming, and partial oxidation [1]. Furthermore, direct conversion of methane into methanol and higher hydrocarbons under oxidative conditions is studied as well [2].

Oxidative coupling of methane (OCM) was first introduced in 1982 by Keller and Bhasin [3] for the production of C2 products—namely, C$_2$H$_4$ and C$_2$H$_6$—in the presence of metal catalysts at atmospheric pressure and temperatures in the range of 700–1300 K. The main challenge of the process is the achievement of high C2 product selectivity at high methane conversion. Since OCM product yields depend considerably on the catalyst used, various researchers have worked with different catalyst formulations in order to maximize yield of C2 species. Most of the catalysts investigated for OCM are oxides of pure or modified transition metals [4], IA or IIA group elements [5], Mn/Na$_2$WO$_4$/SiO$_2$ catalysts [6], or Li/MgO catalysts [7] in the temperature range 1000–1100 K. Other well-known catalysts for OCM are La-doped catalysts such as LaAlO$_3$ [8], La$_2$O$_3$/CeO$_2$ [9], and Sr/La$_2$O$_3$ [10]. However, no particular catalyst has yet met the criteria for a commercial realization of the process.

Alumina has been widely used as a support material in industrial catalysis applications due to its advantageous surface and bulk properties and its ability to promote high metal catalyst stability [11,12]. For instance, Pt/Al_2O_3 catalysts have been investigated for catalytic partial oxidation of methane for the formation of CO and H_2 at temperatures above 1273 K [13]. In this context, unsaturated alumina atoms are considered to play an important role in stabilizing Pt atoms and maintain a high Pt dispersion in Pt/Al_2O_3 catalysts [11,12]. Hohn et al. [14] reported for the first time the functionality of Pt/Al_2O_3 catalysts in OCM at a very high temperature of about 1600 K for short contact times of 20 ms. Thereby, by using a Pt-coated monolith at low CH_4/O_2 ratios, high space velocities, and low N_2 dilution, a selectivity of about 20% of C2 products was achieved. The Pt catalyst was primarily used for the activation of methane via total oxidation at the position near the entrance of the monolithic structure, leading to a rise in the temperature, which is high enough for coupling products to form downstream.

The mechanism of OCM is not yet well understood. Both surface reactions as well as reactions between gaseous species seem to be a prerequisite for achieving significant yields of C2 products. Methane likely interacts with the available oxygen species both in the gas phase and over the catalytic surface [15]. The C–H bond is activated by the oxygen species on the catalyst surface, forming CH_3 radicals desorbing into the gas phase [9,10,15–17]. The combination of CH_3 radicals results in ethane formation in the gas phase and its further dehydrogenation leads to formation of ethylene. The limited yields of desired C2 products is due to consecutive oxidation of C2 products to CO and CO_2 aside from the thermodynamically favored path to syngas [18].

Quiceno et al. [19] studied the partial oxidation of methane over a Pt wire gauze at very short contact times to form CO and H_2, along with the formation of C2 species in the gas phase at elevated pressures. By exploiting molecular beam spectroscopy for their *in situ* study on Pt catalysts, Geske et al. [20] also observed C2 products, above 1350 K. Furthermore, a rise in CH_4 conversion along with C2 products formation was ascertained at a CH_4/O_2 ratio of 0.6, and a maximum selectivity of C_2H_2 of about 17% was observed at approximately 1600 K along with traces of benzene and coke. C2 products formed were attributed to the CH_3 radicals formed in the gas phase at high temperatures above 1400 K among CH_3, CH_2, and CH radicals. In that way, CH_2 and CH radicals were excluded for being the source of C_2H_2 formed.

In the present work, a Pt/Al_2O_3-coated catalytic monolith is used for OCM at short contact times and high temperatures. The objective of this study is a better understanding of the role of catalytic and homogeneous gas phase reactions on the formation of C2 hydrocarbons by using multiscale numerical simulations.

2. Results and Discussion

2.1. Simulation Study of Literature Experimental Results

Lunsford et al. [16] reported that gas-phase reactions predominate over the heterogeneous reactions under oxidative coupling conditions at higher temperatures and facilitate the formation of coupling products. In order to investigate the role of the surface and gas-phase chemistry under oxidative coupling over Pt, simulation studies of experiments were conducted by a two-dimensional flow field description of a single channel of the catalytic monolith using DETCHEM^{CHANNEL} [21,22]. The operating conditions were taken from the pioneering work of Hohn et al. [14]. A detailed gas phase reaction mechanism, PolyMech [23], and/or a multistep surface reaction mechanism, Kahle-Deutschmann [24], were utilized for the numerical simulations.

The simulations were conducted under isothermal conditions, with CH_4/O_2 ratios in the range of 1.4–2.4, at the corresponding, experimentally observed temperature of 1673–1763 K. Two-dimensional numerical simulations were first conducted along the monolithic structure with the total length of 0.01 m.

As shown in Figure 1, the simulation using homogeneous reactions only predict C_2H_2 as the major C2 product and a steady rise in the C2 selectivity with increasing CH_4/O_2 ratios. In contrast with numerically predicted results, the experimentally measured selectivity of C2 products describe an opposite trend, and a gradual decline in C2 selectivity with the rise in CH_4/O_2 ratios is obtained. Thus, it seems very unlikely that only homogeneous chemistry is taking place.
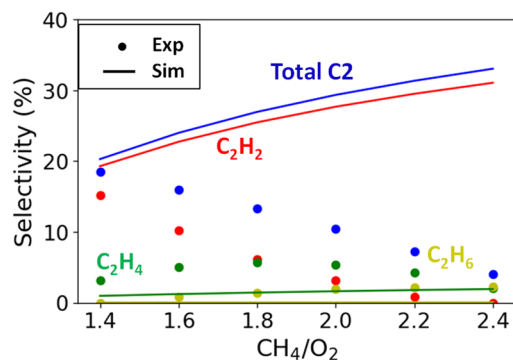
Figure 1. Selectivity of C2 species predicted by simulation considering only kinetics in the gas phase in comparison with experimental results from Hohn et al. [14] (N_2 = 20%, *p* = 1 bar, τ = 20 ms).

In case of considering the surface kinetics only over the length of the catalyst, the simulations predict that CO_2, H_2O, CO, and H_2 are formed as a combination of first total oxidation and partial oxidation downstream where all the oxygen is already gone. The selectivity and conversion of the gas phase species along the monolith for CH_4/O_2 ratios of 1.4 and 2.4 are shown in Figure 2.

| (a) | (b) |
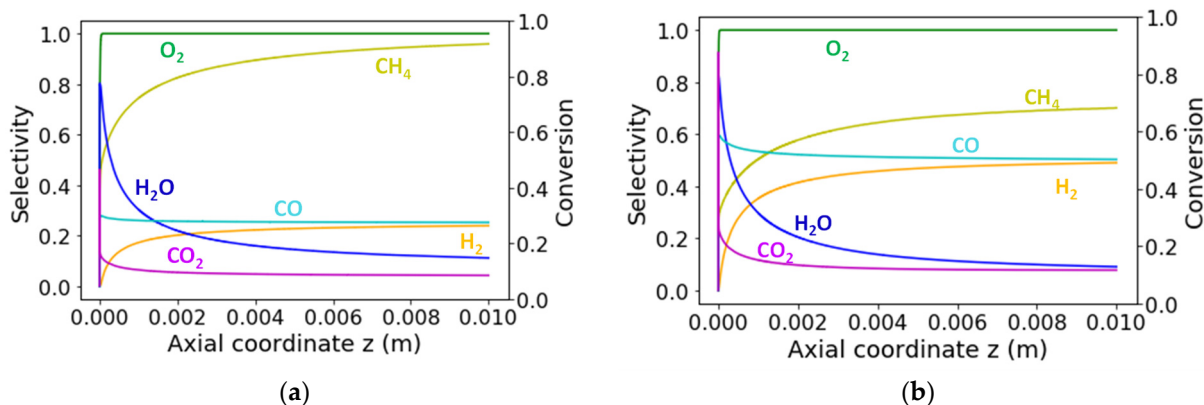
Figure 2. Numerically simulated axial profiles along the monolith channel; (**a**) CH_4/O_2 = 1.4; (**b**) CH_4/O_2 = 2.4 (N_2 = 20%, *p* = 1 bar, τ = 20 ms).

The simulations considering only the surface reactions cannot predict the formation of C2 products, since no coupling reactions are included in the surface mechanism.

Next, we assume that the reaction zone can be divided in two broad zones for further simulations. In the first zone at the front face of the catalyst channel, heterogeneous surface chemistry leads to total oxidation (CO_2, H_2O) and partial oxidation (CO, H_2) products. Initially, a high selectivity of CO_2 and H_2O is observed at the entrance of the catalytic zone with significant O_2 conversion, followed by formation of partial oxidation products along with a rise in CH_4 conversion. At experimental conditions chosen by Hohn et al. [14], this zone is an extremely small area of ca. 0.002 m, where oxygen is available for the oxidation of methane. Since most of the methane is converted over the surface sites, only a small part leads to formation of coupling products in the gas phase in the second zone.

In the second zone, as the oxygen is almost fully consumed, gas phase chemistry becomes significant. At experimental conditions adopted by Hohn et al. [14], at varying CH_4/O_2 ratios, oxygen is fully consumed within the first few millimeters of the catalyst. Further downstream lies the second reaction zone where the gas phase chemistry takes place and ultimately results in the formation of coupling products.

Hence, simulations over the complete length of the catalyst (0.01 m) were conducted at different CH_4/O_2 ratios, with both surface reactions and gas phase reactions, at adiabatic conditions with an inlet reactor temperature of 773 K. For the first 0.002 m of the catalyst (zone 1), only the surface kinetic model was considered and, subsequently, only the gas phase kinetic model was used to simulate the remaining 0.008 m length of the catalyst monolith (zone 2). The simulation results according to this configuration are shown in Figure 3. It is observed that the kinetic simulation follows the experimentally observed trend, where the selectivity of C2s is reduced with increasing CH_4/O_2 ratios. The experimental data suggest C_2H_2 as the major product at CH_4/O_2 ratios < 2, while C_2H_4 is seen as the major product at CH_4/O_2 ratios $\geq$ 2. However, there are deviations in the product distribution predicted by the model, C_2H_2 has been predicted as the major C2 product at all variable CH_4/O_2 ratio conditions. Therefore, further experimental and modeling studies were conducted as a part of this research to understand the underlying rationale.
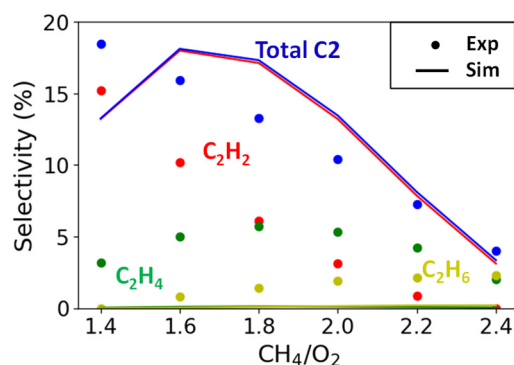
Figure 3. Selectivity of C2 species predicted by simulation considering two-zone kinetic model in comparison with experimental results from Hohn et al. [14] (N_2 = 20%, *p* = 1 bar, τ = 20 ms).

2.2. Simulation Studies with Novel Inhouse Experimental Results

It is also noteworthy that the residence time during the Hohn et al. [14] experiment is of a few milliseconds due to the small channel diameter and the high volumetric flow rate (Table 1). However, at higher space velocities, the length of the first zone is expected to become longer and the second zone with the homogeneous gas phase chemistry is expected to be relatively shifted along the reactor length or even downstream of the monolith, in the empty reactor tube, where the temperature is still very high.

Table 1. Experimental parameters used for the validation of the kinetic model.

Catalyst	2–3% Pt/Al$_2$O$_3$ [1]	2–3% Pt/Al$_2$O$_3$ [1]	1% Pt/Al$_2$O$_3$ [2]	1% Pt/Al$_2$O$_3$ [2]	1% Pt/Al$_2$O$_3$ [2]
Inlet temperature (K)	773	773	773	773	773
Monolith length (m)	0.01	0.01	0.01	0.01	0.01
Monolith diameter (m)	0.018	0.018	0.01	0.01	0.01
Channel diameter (m)	2.3×10^{-4}	2.3×10^{-4}	6.3×10^{-4}	6.3×10^{-4}	6.3×10^{-4}
Flow rate (slpm)	7.5	7.5	5	5–9	6
Velocity (m/s) (at T_{inlet} 773 K)	2.4	2.4	3.6	3.6–6.5	4.3
GHSV ($\times 10^5$ h^{-1})	1.8	1.8	3.7	2.9–7.1	4.5
Residence time (ms)	20	20	10	4–10	8
CH$_4$/O$_2$ ratio	1.7	1.4–2.4	2.0	2.0	1.8–2.4
N$_2$ dilution (%)	20	20	35–80	35	35
Reference	[12]	[12]	this work	this work	this work

[1] 2–3% Pt loading on the alumina foam substrate; [2] 1% Pt loading on the Al$_2$O$_3$ support wash-coated onto the honeycomb monolith.

The two-zone kinetic model proposed above was further evaluated against additional experiments conducted as part of this study with a 1% Pt/Al$_2$O$_3$ catalyst. Simulations were conducted over the maximum length of 0.4 m including not only the monolith, but also the empty reactor tube downstream. DETCHEM^{MONOLITH} [21] was used to model the 0.01 m catalyst and DETCHEM^{CHANNEL} [,21,22] was employed to model the 0.39 m quartz glass tubular reactor downstream of the monolith. Certain experimental parameters were varied over the range of conditions to investigate the optimization of C2s selectivity.

2.2.1. Study of N$_2$ Dilution

Experiments were conducted for variable N$_2$ dilution at a CH$_4$/O$_2$ ratio of 2 with residence time of 10 ms over the in-house prepared 1% Pt/Al$_2$O$_3$ catalyst. Experimentally, the selectivity of C2 species increases to about 6% with the decrement in N$_2$ dilution from 80% to 35%. As shown in Figure 4, the kinetic model predicts the N$_2$ selectivity of total C2 species in good agreement with the experimental values and reproduces the shape of the plot. However, at around 50% dilution, the kinetic model overpredicts the C2 selectivity to almost double the experimental values. The rise in C2 selectivity correlates to the rise in CH$_4$ conversion from 50% to 80% as the N$_2$ dilution was reduced from 80% dilution to 35% dilution. Additionally, C$_2$H$_2$ is observed as major product in the simulation results. Although the model overestimates the temperature, the predicted temperature follows the same trend as observed in the experiments, namely, an increase in temperature with decreasing dilution.
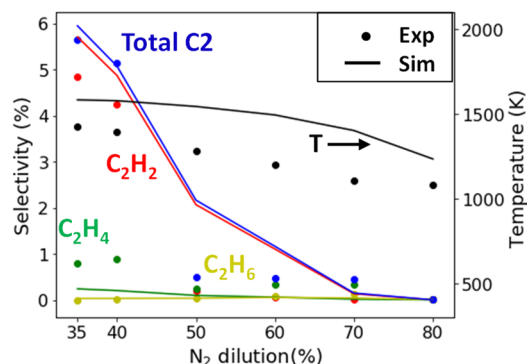
Figure 4. Selectivity of C2 species predicted by simulation considering the two-zone kinetic model in comparison with our experimental result (CH$_4$/O$_2$ = 2, *p* = 1 bar, τ = 10 ms), in dependence of the N$_2$ dilution in the gas flow.

2.2.2. Variation of Flow Rate

The flow rate, i.e., the gas hourly space velocity (GHSV), is known to be a crucial parameter affecting the C2 selectivity. Several authors working with different catalysts ascertained a distinct influence of space velocity over different catalysts on the C2 selectivity by OCM. Witt et al. [25] studied a Rh catalyst and established that 99% of O_2 conversion is desirable for achieving a stable C2 selectivity. Increasing GHSV beyond 4.4×10^5 h^{-1} results in a drop in O_2 conversion and leads to a decline of C2 species. Sarsani et al. [26] discovered that thermal effects and heat loss affect the C2 selectivity apart from the threshold O_2 conversion required for C2 products formation. It was examined that heat loss was dominant at lower GHSV, thereby preventing the autothermal operation of the reactor system. For a La-Ce powder catalyst system, a residence time of 10 ms or less enabled an adiabatic rise in temperature for significant C2 production. Kooh et al. [27] found that higher GHSV enables higher C2 yields by establishing a large difference between furnace temperature and catalyst hotspot temperature. Takanabe et al. [28] employed a $Mn/Na_2WO_4/SiO_2$ catalyst and established the direct association between CH_4 conversion and C2 yields with GHSV. Low GHSV or higher contact time facilitated higher CH_4 conversion and, thereby, higher C2 yields.

During the experiments conducted over the 1 wt.% Pt/Al_2O_3 catalyst at 35% N_2 dilution, a CH_4/O_2 ratio of 2 with varying GHSV conditions and C2 selectivity plateaus at 7% selectivity with 94% CH_4 conversion at space velocity of 4.5×10^5 h^{-1} and declines at higher GHSV. The temperature measured after the catalyst remains almost constant at variable space velocities; the decline in experimentally determined C2 selectivity can be attributed to the decline in CH_4 conversion due to decreasing contact time. Although the numerically predicted kinetic model matches the experimentally determined results well at lower space velocities, at higher space velocities a rise in C2 selectivity is predicted, which differs from the experimentally determined values (Figure 5). Despite the low contact times, the hotspot temperature and the overall CH_4 conversion remain constant. This indicates that even though less CH_4 is expected to be converted in the catalytic zone along the length of monolith, as an effect of increase in GHSV, the model predicts that the overall CH_4 conversion is compensated in the gas phase zone behind the catalyst (Figure 5b), leading to CH_3 radicals and, subsequently, C2 species. However, such an effect cannot be validated in the present experimental campaign, and further work is required to understand the impact of GHSV.

(**a**) (**b**)
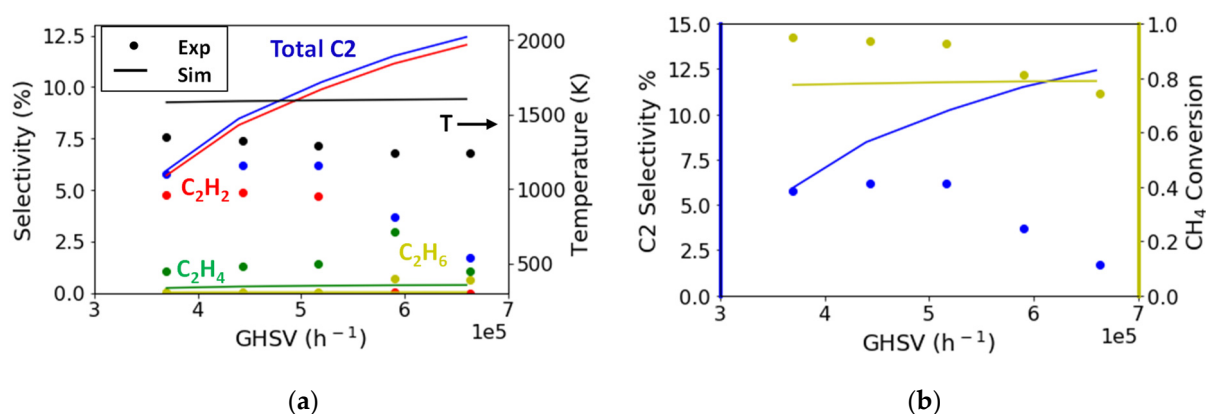
Figure 5. Selectivity of C2 species predicted by simulation considering two-zone kinetic model in comparison with our experimental result as a function of GHSV (CH_4/O_2 = 2, *p* = 1 bar, 20% N_2). (**a**) C2 selectivity and temperature downstream the monolith; (**b**) C2 selectivity and CH_4 conversion.

2.2.3. Variation in CH_4/O_2 Ratio

Experiments were conducted for variable CH_4/O_2 ratios from 1.8–2.4, under conditions with 35% N_2 dilution, space velocity of 4.5×10^5 h^{-1}, and corresponding

residence time of 8 ms over 1% Pt/Al_2O_3 catalyst. Simulations conducted including only surface kinetics along the catalyst depict that due to the very low residence time, the oxygen is not fully consumed in the catalytic zone up to the end of the monolith. Unlike the Hohn et al. [14] experiments, oxygen is rather fully converted in the gas phase zone after the monolith. Hence, the two-zone model simulations were configured so that the surface chemistry was considered along the catalyst's overall length (0.01 m) and the gas phase chemistry was considered along the empty tube reactor downstream of the monolithic catalyst (0.39 m). In Figure 6, the kinetic simulations envision the experimentally measured C2 selectivity for a CH_4/O_2 ratio ≥ 2 quite closely. However, at a CH_4/O_2 ratio < 2, the kinetic model overpredicts the C2 selectivity and predicts the maximum C2 selectivity at a CH_4/O_2 ratio of 1.6 with 14% C2 selectivity and 92% CH_4 conversion. Experimentally, the maximum C2 selectivity of 7% with 94% CH_4 conversion is observed at a CH_4/O_2 ratio of 2.0. Kinetic study at a CH_4/O_2 ratio of 1.4 is estimated to explain the reduction in C2 selectivity observed at a CH_4/O_2 ratio of 1.8 experimentally. Thus, to have a better understanding, the axial profiles for conversion of reactants and formation of products are discussed in more detail in the next section.
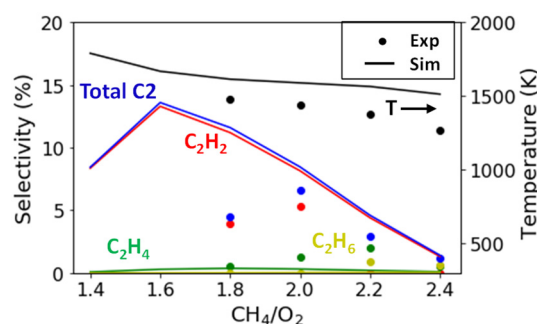
Figure 6. Selectivity of C2 species predicted by simulation considering two-zone kinetic model in comparison with our experimental result in dependence of the CH_4/O_2 ratio in the gas flow (N_2 = 35%, *p* = 1 bar, τ = 8 ms).

2.3. Catalytic Reaction Kinetics over the Monolith

During the experiments, the reactor's final product composition was measured by analyzing the effluent gas stream's composition. While these results allow for optimizing the process parameters with respect to maximum CH_4 conversion and C2 selectivity, spatial information on selectivity and conversion along the length of the reactor are of major relevance in order to better understand the reaction hierarchy. Simulations of the reactor model coupled with detailed kinetic models were used to determine the molar fractions of the products as the reactant gases are converted inside the reactor, with an emphasis on the catalytic zone.

In Figure 7, the two-dimensional temperature profile across the monolith, obtained using DETCHEM^{MONOLITH}, describes a rise in temperature, which is observed at the onset of the catalyst surface. However, for lower CH_4/O_2 ratios, the maximum temperature reported across the monolith is substantially higher. Furthermore, axial profiles of reactants and products over the Pt catalyst, obtained using the Kahle-Deutschmann kinetic model, are shown in Figure 8. Simulation results for variable CH_4/O_2 ratios 1.4, 1.6, and 2.4 are computed with an initial reactor temperature of 773 K. Under all three cases, a rise in temperature is observed in the first 0.002 m of the catalyst surface along with a fast decrease in the mole fractions of methane and oxygen due to high catalytic activity of Pt in the oxidation reactions. Based on the profiles obtained for variable CH_4/O_2 ratios, we can establish two zones over the catalyst length: A total oxidation (combustion) zone and a partial oxidation/steam reforming zone.
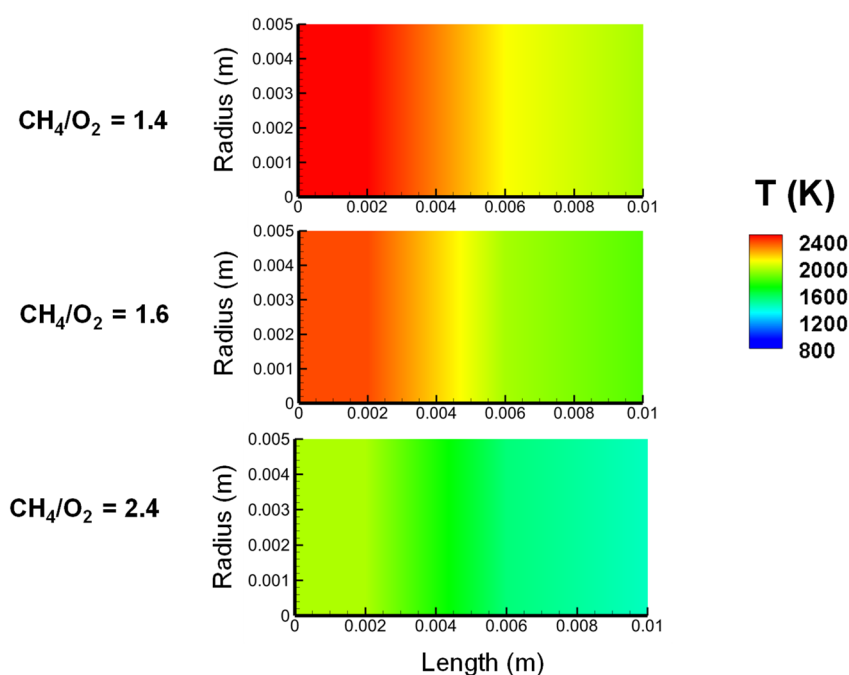
Figure 7. Temperature distribution across the monolith of length 0.01 m and radius 0.005 m coated with 1 wt.% Pt/Al_2O_3 at variable CH_4/O_2 ratios (N_2 = 35%, *p* = 1 bar, τ = 8 ms).
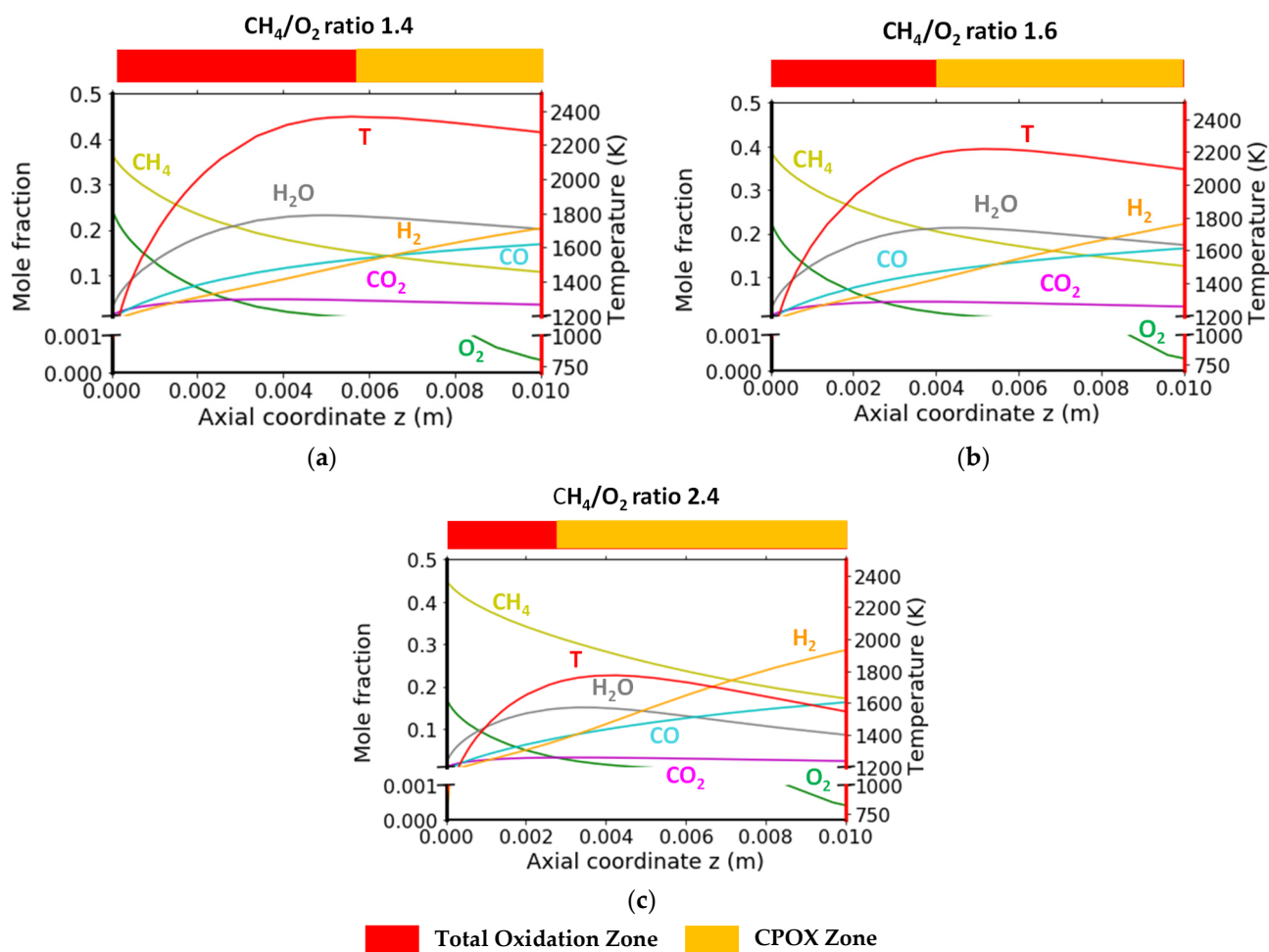
Figure 8. Numerically simulated axial profiles along the catalytic monolith of length 0.01 m at (**a**) CH_4/O_2 ratio = 1.4; (**b**) CH_4/O_2 ratio = 1.6; (**c**) CH_4/O_2 ratio = 2.4. *p* = 1 bar, τ = 8 ms).

Total oxidation (combustion) zone: The simulation suggests an initial combustion zone under both low fuel (CH_4/O_2 = 1.4) and high fuel (CH_4/O_2 = 2.4) input conditions, on the interaction of gases with the catalyst surface. CO_2 and steam, which are produced by complete oxidation of methane, are created in the first few millimeters of the catalyst surface. As the O_2 is being consumed due to complete oxidation at the catalyst's starting length, the exothermic combustion reaction results in a pronounced temperature increase. The combustion reactions are dominant for approximately 0.006 m from the inlet of the monolith when the fuel inlet condition is low (CH_4/O_2 = 1.4), and the respective temperature reaches 2400 K. Under high fuel (CH_4/O_2 = 2.4) conditions, the temperature increase obtained by the simulations is 1750 K. However, the combustion zone is shorter (z = 0.003 m) followed by the reactor zone where the catalytic partial oxidation zone is dominant.

A sensitivity analysis of the Kahle-Deutschmann mechanism [24] (supplemented in Appendix A) allows us to analyze the major pathways for CH_4 conversion and formation of products over the Pt catalytic surface under adiabatic conditions at a CH_4/O_2 of 1.4. The following are the primary reactions on the catalyst's surface in the total oxidation zone:

i. Methane adsorption with hydrogen atom abstraction (Figure A2a):

$$CH_4 \rightarrow CH_4(s) \rightarrow CH_3(s) + H(s) \tag{1}$$
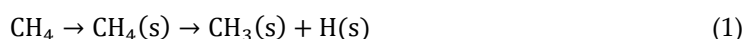
ii. The process of water formation (Figure A2b):

$$O(s) + H(s) \rightarrow OH(s) \tag{2}$$

$$OH(s) + H(s) \rightarrow H_2O(s) \rightarrow H_2O \tag{3}$$
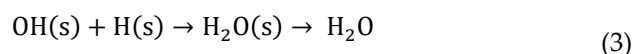
iii. CO_2 desorption (Figure A2c):

$$CO_2(s) \rightarrow CO_2 \tag{4}$$

CPOX (catalytic partial oxidation) zone: In this zone, H_2 is generated on the catalytic surface by steam reforming and partial oxidation of methane to syngas near the exit of the monolith under low fuel input conditions (CH_4/O_2 = 1.4). Under high fuel conditions (CH_4/O_2 = 2.4), the total oxidation zone is shorter and the CPOX zone is prominent, which results in an increase in CO and H_2 mole fractions throughout the catalyst length. In the case of high fuel circumstances (CH_4/O_2 = 2.4), the dominant CPOX and steam reforming results in a relatively lower hotspot temperature near the exit of the monolith (1500 K). Under both low (CH_4/O_2 = 2.4) and high (CH_4/O_2 = 2.4) fuel conditions, the available oxygen is not completely utilized on the catalyst surface.

The following are the primary reactions on the catalyst's surface in the CPOX zone:

i. Carbon monoxide is formed on the surface (Figure A2d):

$$CO_2(s) + C(s) \rightarrow CO(s) + CO(s) \tag{5}$$
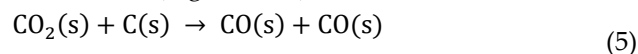
ii. The desorption of hydrogen atoms after recombination of hydrogen atoms (formed in reaction (1)) on the catalyst's surface (Figure A2e):

$$H(s) + H(s) \rightarrow H_2(s) \rightarrow H_2 \tag{6}$$
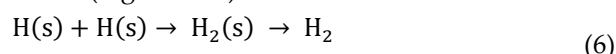
In the simulations shown in this section, only the surface reactions are considered and the formation of C2 products is not predicted, because coupling reactions are not considered on the surface. However, when both the surface and gas phase kinetics are considered in the kinetic model, C2s are formed at a thermally insulated empty reactor tube downstream of the monolith. Additionally, the presence of O_2 at the exit of the monolith is of importance in all cases, as O_2 is not fully consumed along the monolithic channel (Figure 8). The remaining CH_4 and O_2 at the exit of the catalyst play a crucial role

on the coupling of methane in the gas phase, which is discussed in detail in the next section.

2.4. Homogeneous Reaction Kinetics after the Monolith

In the previous section, we described that along the monolith channel, zones of dominating reactions are predicted by simulations. At the empty reactor tube after the monolith exit, the coupling zone develops, where some of the residual methane is transformed into coupling products. Figure 9 depicts the predicted mole fractions of primary products and additional C2 species generated as a function of axial position up to the exit of the insulated empty tube reactor at z = 0.4 m. From the profiles obtained, we can also establish different reaction zones based on dominant products over the reactor length in the gas phase zone. Different reactions are dominant in the gas phase depending on the inlet CH_4/O_2 ratios.
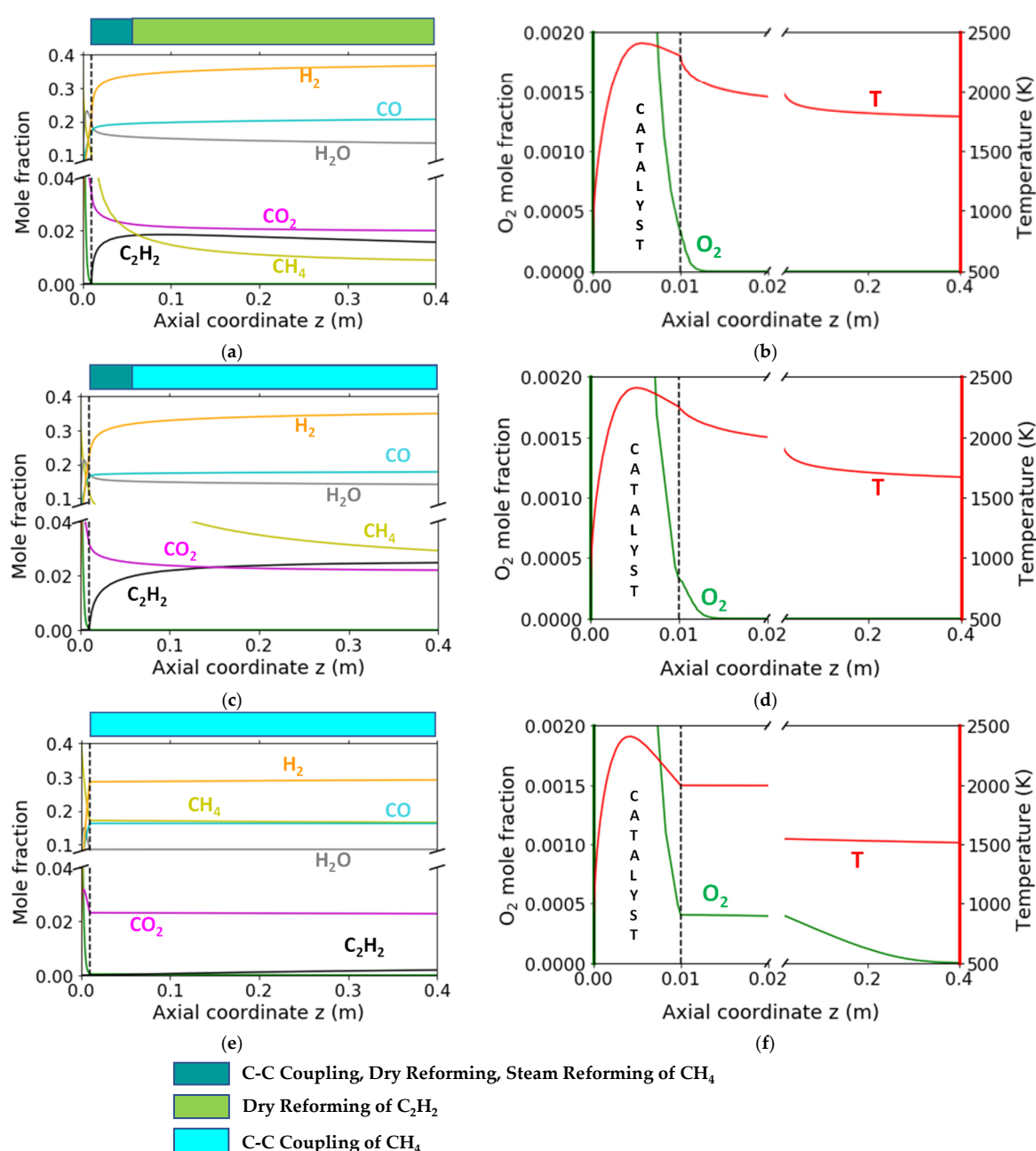
Figure 9. Numerically simulated axial profiles downstream of the catalytic monolith over the length of 0.4 m with (**a**) mole fractions at CH_4/O_2 ratio = 1.4; (**b**) temperature and O_2 mole fraction at CH_4/O_2

ratio = 1.4 at (**c**) mole fractions at CH_4/O_2 ratio = 1.6; (**d**) temperature and O_2 mole fraction at CH_4/O_2 ratio = 1.6 at (**e**) mole fractions at CH_4/O_2 ratio = 2.4; (**f**) temperature and O_2 mole fraction at CH_4/O_2 ratio = 2.4 (N_2 = 35%, *p* = 1 bar, τ = 8 ms).

Coupling zone: Under low input fuel conditions (CH_4/O_2 = 1.4, CH_4/O_2 = 1.6), the coupling zone follows the partial oxidation at the end of the catalyst surface due to very fast kinetics of available O_2 at high temperature. At the catalyst outlet, the gas phase temperature is high as 2300 K (CH_4/O_2 = 1.4) and 2100 K (CH_4/O_2 = 1.6) and unreacted methane and oxygen interact with the active radicals in the gas phase and form CH_3 radicals (Figure 9b,d). For all fuel conditions, C2 formation is attributed to the following reactions:

i.　The OH radicals desorbed from the catalytic surface react with methane to generate water:

$$CH_4 + OH^{\cdot} \rightleftharpoons CH_3^{\cdot} + H_2O \tag{7}$$

ii.　On complete consumption of available oxygen, methane releases methyl radicals by H-atom abstraction (reaction (8)) or initiation/thermal decomposition (reaction (9))

$$CH_4 + H^{\cdot} \rightleftharpoons CH_3^{\cdot} + H_2 \tag{8}$$

$$CH_4 \, (+M) \rightleftharpoons CH_3^{\cdot} + H^{\cdot} \, (+M) \tag{9}$$

Further, a reaction flow analysis (RFA) is performed for the PolyMech mechanism at 1673 K, CH_4/O_2 of 1.4, 35% N_2 dilution and is supplemented in Appendix A. The RFA (Figure A1) suggests that due to the fast kinetics and low activation energy of reaction (7) at high temperature, reaction (7) predominates over reaction (8) and (9). Thereby, CH_3 radicals are formed in the gas phase, which is the source initiator for the coupling products formation. CH_3 radicals combine together at high temperature to form C_2H_6. The concentration of C_2H_6 is negligible, as it is quickly consumed at high temperature to form C_2H_4 (Figure A1). By interacting with CH_3 and H radicals, C_2H_4 is rapidly transformed to C_2H_2, which is a more thermodynamically stable under these conditions due to its Gibbs free energy [29,30].

At high fuel conditions (CH_4/O_2 = 2.4), a shift in the coupling zone is observed along the length of the reactor. Initially, C_2H_6 is formed, which is subsequently transformed into C_2H_4 and C_2H_2 at high temperatures. A stable concentration of C_2H_2 is visualized at the end of the reactor (Figure 9e). Here, the available O_2 combines with a H radical to form metastable HO_2 radicals (reaction (10)), which act as a reducing agent [31] and inhibit the further conversion of CH_4 (Figure 9f).

$$O_2 + H^{\cdot} + M \rightleftharpoons HO_2^{\cdot} + M \tag{10}$$

Methane reforming zone: Methane reforming is also dominant in the gas phase zone in the case of low input fuel conditions (CH_4/O_2 = 1.4, CH_4/O_2 = 1.6) but does not take place in a discrete zone (Figure 9a,c). Along the axial position of the reactor, both steam reforming (SR) and dry reforming (DR) of methane is contemplated along with the pyrolytic coupling zone of methane in a short zone in the gas phase [29,30]. Reforming is the endothermic zone that occurs after the initial formation of CH_3 radicals under the presence of O-containing species. In Figure 10, the two-dimensional concentration profiles at CH_4/O_2 of 1.4 and CH_4/O_2 of 1.6 over the homogeneous reforming zone are shown. Figure 10 describes that decline in temperature as well as CO_2 and H_2O concentrations along with the rise in CO and H_2 can be attributed to the onset of the endothermic reforming reactions.
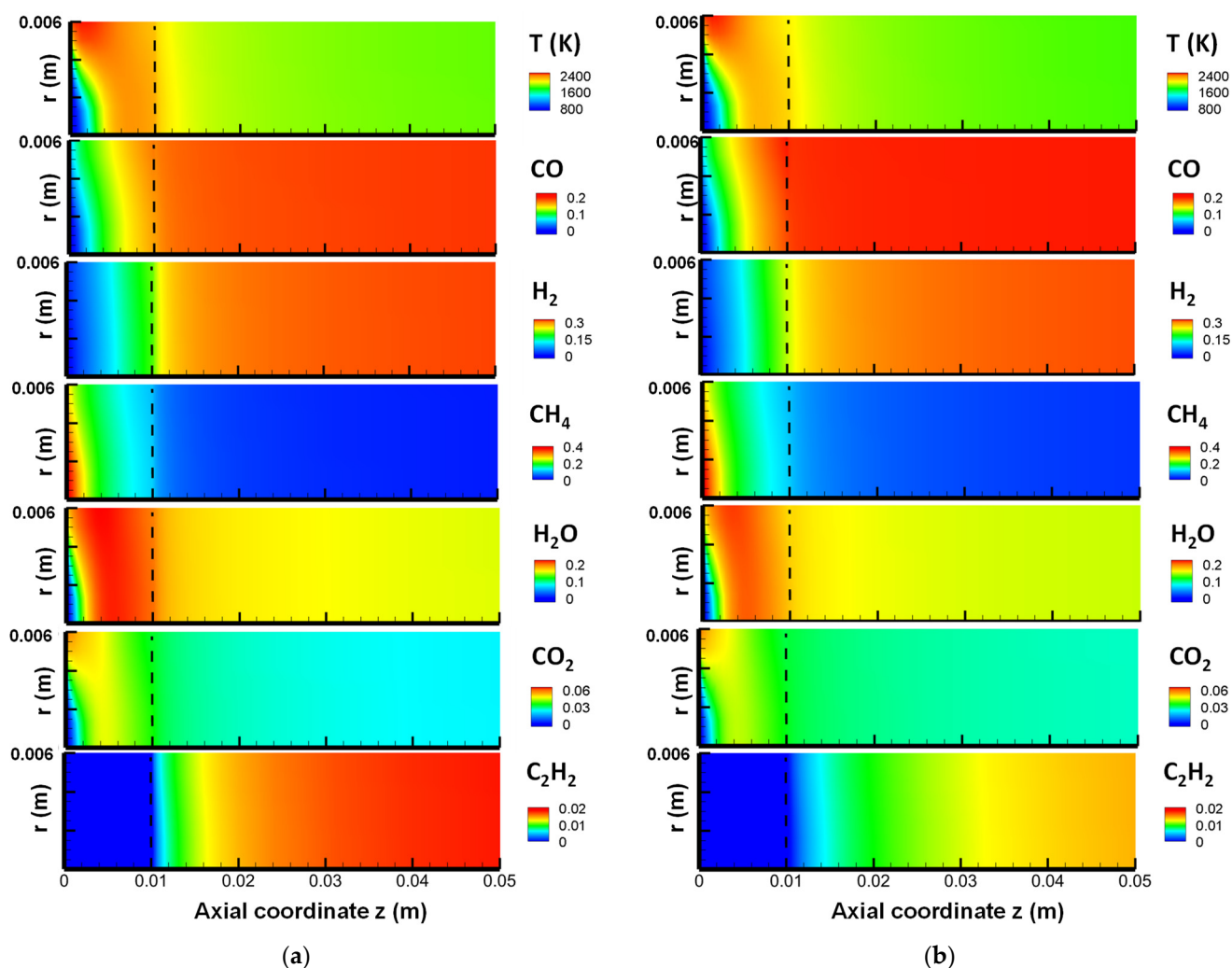
Figure 10. Numerically simulated two-dimensional profiles of temperature and mole fractions of reactants and major products downstream of the catalytic monolith over the homogeneous reforming zone (the length of approximately 0.05 m, N_2 = 35%, *p* = 1 bar, τ = 8 ms): (**a**) at CH_4/O_2 ratio = 1.4; (**b**) at CH_4/O_2 ratio = 1.6.

In homogeneous steam reforming of methane, H_2 and CO are the main products, but small fractions of C2 are produced as byproducts [32,33]. From a mechanistic point of view, the available H_2O generates OH radicals that react with methane (reaction (7)) to generate the desired CH_3 radicals for C2 formation [34]. Simultaneously, the H_2O concentration decreases, while the concentration of CO and H_2 increases. The decline in H_2O mole fraction along the axial length of reactor downstream of the monolith, along with the rise in C_2H_2, CO, and H_2 mole fractions over the reforming zone, can also be visualized in Figure 10.

In the context of homogeneous dry reforming of methane, Angeli et al. [35] observed that C2 products are formed as byproducts along with CO and H_2 at a temperature of 1623 K. Thus, dry reforming enhances the C2 products formation at high temperature. CO_2 is converted at a high pace, with the major reaction pathway being its interaction with hydrogen atoms to generate CO and an OH radical.

$$CO_2 + H^{\cdot} \ \rightarrow \ CO + OH^{\cdot} \tag{11}$$

As a consequence, CO_2 promotes the formation of OH radicals in the dry reforming of methane, thereby, increasing the reactivity of the primary reaction pathway (reaction (7)) for C2 formation [36]. The decline in CO_2 mole fraction along with rise in C_2H_2 is more

profound in the case of a CH_4/O_2 of 1.4, as compared with CH_4/O_2 of 1.6 (Figure 10). Thus, it can be postulated that reforming has a stronger influence at lower CH_4/O_2 ratios.

Acetylene reforming zone: At substantially higher temperatures achieved at low fuel conditions ($CH_4/O_2 = 1.4$), the interaction of C_2H_2 with OH radicals causes the observed decrease in C_2H_2 and an increase in CO mole fractions (Figure 9a). Once the proportion of OH radicals generated as a result of the reaction (11) is elevated, acetylene interacts with the OH radicals to form CH_2CO, which then decomposes into CO and methyl radicals (reaction (12)):

$$C_2H_2 + OH^{\cdot} \;\rightarrow\; CH_2CO + H^{\cdot} \tag{12}$$

$$CH_2CO + H^{\cdot} \;\rightarrow\; CO + CH_3^{\cdot} \tag{13}$$

The C_2H_2 conversion rate is affected by the CO_2/CH_4 ratio. After notable methane conversion, high CO_2 concentrations promote the reforming of C_2H_2. Moreover, Savchenko et al. [35] studied homogeneous dry reforming of methane and found that with higher initial CO_2/CH_4 ratio conditions, C_2H_2 formed was faster converted to CO, leading to its decline (Figure 11b). In our experiments, due to the long total oxidation zone, the maximum CO_2 concentration at the outlet of the monolith is obtained for an initial CH_4/O_2 ratio of 1.4. Furthermore, the higher CH_4 conversion achieved at a CH_4/O_2 ratio of 1.4 causes the rise in CO_2/CH_4 ratio along the length of the reactor downstream of the monolith, as shown in Figure 11a, thereby declining C_2H_2 mole fraction.

(**a**) (**b**)
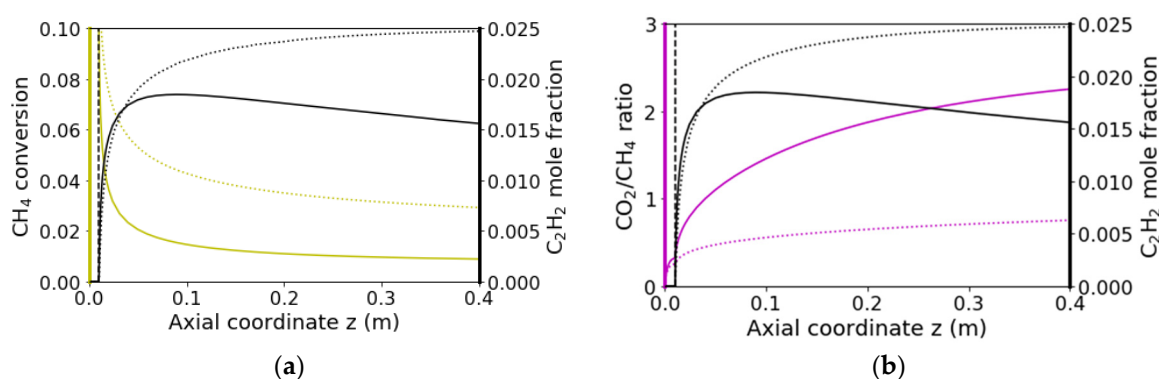
Figure 11. Numerically simulated C_2H_2 mole fraction along the axial length of the reactor of 0.4 m in the gas phase and its dependence on (**a**) CH_4 conversion (**b**) CO_2/CH_4. Solid line, CH_4/O_2 ratio = 1.4; dotted line, CH_4/O_2 ratio = 1.6.

The relatively lower endothermicity of C_2H_2 reforming reaction and the exothermic water gas shift reaction are responsible for the fact that the temperature profile is not strongly affected in the gas phase.

$$CO + H_2O \;\rightleftharpoons\; CO_2 + H_2 \tag{14}$$

3. Materials and Methods

3.1. Experimental

3.1.1. Catalyst Preparation

The 1% Pt/Al_2O_3 catalyst powder was prepared via incipient wetness impregnation (IWI) [37]. For this, the commercial Al_2O_3 support (Puralox, Sasol, Sandton, South Africa) was calcined for 5 h at 700 °C and the crystalline $(NH_3)_4Pt(NO_3)_2$, which served as Pt precursor (Alfa Aesar, Haverhill, MA, USA) was dissolved in purified water equal to the pore volume of the calcined Al_2O_3 before impregnation. After 2 h of drying at 70 °C and calcination of the received powder at 823 K for 5 h under static air, the powder catalyst

was wash-coated onto cordierite monolithic honeycombs using the methodology previously described by Karinshak et al. [38]. The resulting honeycomb catalyst samples with a cell density of 400 cpsi, a length of 0.01 m, and a diameter of 0.01 m exhibited a noble metal loading of 30 g/ft^3. The noble metal dispersion of 47% was measured by means of CO chemisorption, as described in detail by Chan et al. [39].

3.1.2. Reactor Setup and Experimental Procedure

The experiments were performed in a quartz glass tubular reactor, which was placed in a furnace (HST 12/400, Carbolite, Sheffield, UK), enabling heating, and the reactor's reaction zone was additionally wrapped with thermal insulation to ensure adiabatic operation. Before flowing into the reactor, the feed gas mixture consisting of methane, oxygen, and nitrogen was premixed and preheated to 463 K, while the furnace temperature itself was kept constant at 773 K. Experiments were performed at atmospheric pressure and at flowrates of minimum 5 slpm (standard liters per minute), resulting in residence times of milliseconds in the monolithic catalyst samples. The quartz glass tubular reactor, which is schematically depicted in Figure 12, is about 0.6 m long. Two thermocouples were placed—one inside the monolith and one after the monolith— to measure the temperature at the catalyst surface and the temperature after the catalyst in the reactive zone, respectively.
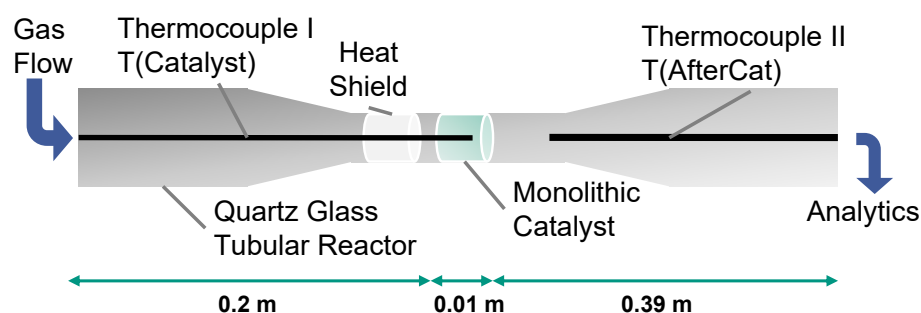
Figure 12. Schematic illustration of the experimental setup.

The coated monolithic catalyst was placed 0.2 m downstream of the reactor inlet. An uncoated cordierite honeycomb (diameter, 0.01 m; length, 0.01 m), placed upstream of the coated catalyst, served as a heat shield and ensured optimal heat transfer. A small space of approximately 0.005 m was kept between the heat shield and the coated monolith catalyst to avoid flow disturbance at the front entrance of the catalytic monolith.

Experimental results by Hohn et al. [14] were used as a preliminary investigation to evaluate and understand the surface and gas phase chemistry involved in the catalytic coupling of methane under oxidative conditions. Similar to the present study, the authors used a quartz glass tubular reactor with a diameter of 0.018 m and length of 0.4 m. The study employed alumina foam impregnated with Pt, resulting in a Pt loading of 2–3% on the structured substrate. To prevent radiation losses, an uncoated monolith was placed in front of the catalyst and the reactor was insulated from outside in order to allow an operation under adiabatic conditions.

The literature data of the study by Hohn et al. [14] and the experiments of the present study conducted with a 1% Pt/Al$_2$O$_3$ catalyst were utilized for the validation of the kinetic model. Table 1 summarizes the experimental conditions used for the comprehension and validation of the model. Experiments over a wide range of input parameters including catalyst metal loadings, space velocities, residence times, N$_2$ dilution, and catalyst dimensions were selected.

3.2. Model Description and Numerical Simulation

In multiscale modelling of heterogeneous catalytic reactors, the steps involved in the process can be predicted starting with the reaction mechanism at atomic scale, reaction rates and adsorption and diffusion processes over the catalyst surface, and reaction rates in the gas-phase [40]. The numerical simulations in this work include the catalytic performance simulations of the chemical system under reaction conditions by coupling the 2D DETCHEM^CHANNEL [21,22] reactor model with the elementary step-based kinetic models of gas phase and surface reactions. Further, DETCHEM^MONOLITH [21] simulations are conducted over honeycomb catalyst to include transient conditions. DETCHEM^MONOLITH models the transient temperature field, by a thorough simulation of representative channels using DETCHEM^CHANNEL code.

3.2.1. Mathematical Model

In the 2D reactor model (DETCHEM^CHANNEL), the flow field of a cylindrical channel of the monolith is calculated under steady-state conditions by solving parabolized Navier-Stokes equations in the boundary layer approximation:

Continuity Equation

$$\frac{\partial(r\rho u)}{\partial z} + \frac{\partial(r\rho v)}{\partial r} = 0 \tag{15}$$

Axial momentum equation

$$\frac{\partial(r\rho u^2)}{\partial z} + \frac{\partial(r\rho uv)}{\partial r} = -r\frac{\partial p}{\partial z} + \frac{\partial}{\partial r}\left(\mu r\frac{\partial u}{\partial r}\right) \tag{16}$$

Conservation of energy

$$\frac{\partial(r\rho uh)}{\partial z} + \frac{\partial(r\rho vh)}{\partial r} = u\frac{\partial p}{\partial z} + \frac{\partial}{\partial r}\left(\lambda r\frac{\partial T}{\partial r}\right) - \frac{\partial}{\partial r}\left(\sum_s rj_s h_s\right) \tag{17}$$

Species continuity equation

$$\frac{\partial(r\rho uY_s)}{\partial z} + \frac{\partial(r\rho vY_s)}{\partial r} = -\frac{\partial}{\partial r}(rj_s) + r\dot{\omega}_s \tag{18}$$

where r is the radial coordinate, z is the axial coordinate, ρ is the density, u is the axial component of velocity, v is the radial component of velocity, λ is the thermal conductivity, p is the pressure, Y_s is mass fraction of the species s, μ is the viscosity, j_s is the radial flux of species s, $\dot{\omega}_s$ is the gas-phase production rate of species s, and h_s is the enthalpy density of the species s.

DETCHEM^MONOLITH solves the unsteady-state two-dimensional heat conduction equations:

$$\rho c_p \frac{\partial T}{\partial t} = \frac{\partial\left(\lambda_{ij}\frac{\partial T}{\partial x_j}\right)}{\partial x_i} + q \tag{19}$$

where t is the time, T temperature, ρ density, c_p is the heat capacity, λ_{ij} tensor of heat conductivity, and q is heat source term for interaction within the channels.

$$q = -\sigma\frac{dH_{channel}}{dx} \tag{20}$$

where σ is the channel density (in channels per cross-sectional area).

Neumann boundary conditions are applied:

$$-\lambda\frac{\partial T}{\partial n}\bigg|_{wall} = \varphi \tag{21}$$

$$\varphi = c(T - T_{surr}) + \epsilon\sigma_{SB}(T^4 - T_{surr}^4) + \varphi_{const} \tag{22}$$

where σ_{SB} is the Stefan-Boltzmann constant, c is the heat transfer coefficient, ϵ is the emissivity, and T_{surr} the surrounding temperature.

The state of the reactive catalytic surface is described by the mean-field model, i.e., in terms of coverages. The coverage, θ_s, can be defined as the fraction of surface sites covered with surface species or adsorbed gas phase species

$$\theta_s = \frac{c_s \sigma_s}{\Gamma} \tag{23}$$

where c_s is the concentration of species s, σ_s is the number of sites occupied by one molecule of the species s, and Γ is the surface site density. For Pt, the surface density was taken as 2.72×10^{-5} mol m^{-2} [24].

A surface reaction can be represented as

$$\sum_{i=1}^{N_g+N_s} v'_{ik} A_i \;\rightarrow\; \sum_{i=1}^{N_g+N_s} v''_{ik} A_i \tag{24}$$
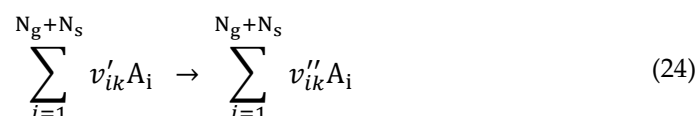
where N_g is the number of gas phase species, N_s is the number of surface species, and $v_{ik} = v'_{ik} - v''_{ik}$ is the stoichiometric coefficients. The total molar production rate $\dot{s}_i$ of surface species i on the catalyst is calculated by

$$\dot{s}_i = \sum_{k=1}^{K_s} v_{ik} k_{\text{f}k} \prod_{j=1}^{N_g+N_s} c_j^{v'_{jk}} \tag{25}$$

The kinetics of the elementary surface reactions are represented by a modified Arrhenius equation:

$$k_{\text{f}k} = A_k T^{\beta_k} \exp\left(\frac{-E_{\text{a},k}}{RT}\right) \prod_i \exp\left(\frac{\epsilon_{ik}\theta_i}{RT}\right) \tag{26}$$

where $k_{\text{f}k}$ is the reaction rate coefficient, A_k is the preexponential factor, β_k is a temperature exponent, $E_{\text{a},k}$ is the activation energy, ϵ_{ik} is a coverage-dependent activation energy, and R is the gas constant [21].

3.2.2. Reaction Flow Analysis

A reaction flow analysis (RFA) identifies and describes the major successive pathways for the formation of products and utilization of reactants in a chemical reaction mechanism based on the rate of species production. In this work, the methodology was adopted from Gossler et al. [41]. The integral reaction flow analysis identifies the contribution of the most important reactions throughout the time interval considered.

3.2.3. Sensitivity Analysis

A sensitivity analysis identifies rate-determining steps as well as the essential parameters of the process. The approach adopted by Herrera Delgado et al. [42] is utilized for sensitivity analysis studies over the surface mechanism. In its most primitive form, a completely mixed reactor with only surface reactions operating at a constant temperature is examined.

The change in the amount n_i of species is given by

$$\frac{\mathrm{d}n_i}{\mathrm{d}t} = A_{\text{cat}} \dot{s}_i \tag{27}$$

where A_{cat} is the catalytic surface area.

A time-dependent sensitivity coefficient $E_{i,k}(t)$ is defined as the change in the number of species i in relation to a relative change in the rate coefficient $k_{\text{f}k}$,

$$E_{i,k}(t) = \frac{\partial n_i(t)}{\partial \ln k_{fk}} \tag{28}$$

Thus, the time development of the sensitivity coefficient is solved by inserting Equations (25) and (27) into Equation (28):

$$\frac{dE_{i,k}(t)}{dt} = A_{\text{cat}} v_{ik} k_{fk} \prod_{j=1}^{N_g+N_s} c_j^{v'_{ik}} + A_{\text{cat}} \sum_{l=1}^{K_s} v_{il} k_{fl} \left(\prod_{j=1}^{N_g+N_s} c_j^{v'_{jl}} \right) \left(\sum_{j=1}^{N_g+N_s} v'_{ik} \frac{E_{j,l}}{n_j} \right) \tag{29}$$

As a result, the sensitivity coefficient describes the contribution of the kth reaction to the generation of species i.

3.2.4. Chemical Reaction System

Gas Phase Reaction Models

Four different gas phase homogeneous models were initially considered in this work for the oxidative coupling of methane at high temperatures. The first mechanism was based on the widely used GRI Mech 3.0 [43], developed for natural gas by the Combustion Laboratory at the University of California, Berkeley. The mechanism consists of 53 species and 325 reactions to describe the combustion of natural gas in the temperature range of 1000–2500 K at 0.1–10 bar and for equivalence ratios of $\varphi = 0.1$–5.

The second was the detailed mechanism by Healy et al. [44] with 289 species and 3128 reactions. The Healy-Curran model has been validated for oxidation of methane and propane mixtures for the temperature range of 740–1550 K at compressed gas pressures of 10–30 bar and for varying equivalence ratios of 0.3–3.0 in a high-pressure shock tube and in a rapid compression machine.

Another mechanism for ethane oxidation with 180 species and 2069 reactions based on work by Dean's group [45] was applied as well. This mechanism was validated for a wide range of conditions with temperatures varying between 700 K and 1800 K, pressures of approximately 1–10 bar, and equivalence ratios of $\varphi = 0.1$–1.5. The range of experiments include a high-pressure flow reactor, shock tube studies, and low-pressure flame experiments.

A relatively smaller mechanism with 58 species and 588 reactions, PolyMech by Porras et al. [23], was used for the simulations as well. The mechanism includes both oxidative and pyrolytic reaction pathways for the conversion of methane and the formation of aromatics up to benzene. Fuel-rich methane/dimethyl ether/air mixtures (fuel–air equivalence ratio $\varphi = 1$–20) were used for its validation in the temperature range of 630–1500 K, with a pressure of 1–20 bar in a shock tube and in a rapid compression machine experiment.

The homogeneous gas phase models were compared for the experimental conditions used by Hohn et al. [14] at a CH_4/O_2 ratio of 1.7, 20% N_2, and at a residence time of 20 ms. DETCHEM$^{\text{CHANNEL}}$ [21,22] simulations were conducted isothermally at the experimentally observed temperature of 1673 K. These reaction conditions were selected for the evaluation of the gas phase kinetic models because the temperature is very high; therefore, the gas-phase reactions are expected to take place in high rates. Hohn et al. [14] compared the experimental data with that of the model presented by Dean et al. [45]. However, the large number of defined species and chemical reactions act as an impediment in its utilization in further studies. Among the four mechanisms studied in this work, the Healy-Curran model [44] and the PolyMech mechanism [23] predict the experimentally measured end-of-pipe C2 selectivity and CH_4 conversion considerably well. However, neither of the two models was able to accurately describe the product distribution of C2 species (C_2H_6, C_2H_4, C_2H_2). The PolyMech [23] mechanism has the advantage of including a relatively smaller number of species and elementary reactions, thus, it requires less computational time for the numerical simulations. Furthermore, PolyMech has been

successfully used for the simulation of gas phase dry reforming experiments at high temperature [35] and, thereby, was selected to be used in this work.

Surface Reaction Models

Platinum-based catalysts over support materials such as CeO_2 or Al_2O_3 are known to be active in the oxidation of various hydrocarbons. In this study, two heterogeneous detailed kinetic models for platinum catalyst were used to understand and evaluate the role of the catalyst in the oxidative coupling of methane at high temperatures. In the first mechanism, Quiceno et al. [19] described the high activity of platinum for partial oxidation of methane at elevated temperatures. The mechanism, consisting of 21 species and 36 reactions, has been validated by experiments in a platinum wire gauze reactor at 1.3 bar and temperatures ranging from 700–1100 K (CH_4/O_2 = 2.5, diluted by 80% He, residence time τ = 36 s). Above 1200 K, a significant amount of hydrogen is formed, while steam is observed at lower temperatures. C2 species are not included in this mechanism. In the second mechanism, the kinetics of methane dry reforming at high temperatures over platinum are addressed by the Kahle-Deutschmann model [24]. The mechanism, comprising 22 species and 58 reactions, was validated at a temperature of 1123–1273 K and a pressure of 20 bar, for experiments carried out over a catalytic bed of Pt-containing pellets with a CH_4/CO_2 ratio of 1.0.

The two heterogeneous models were examined for the experimental conditions used by Hohn et al. [14]. Both models predict equivalent catalytic activity leading to similar composition of reaction products and elevation in temperature due to exothermic reactions. However, among the two kinetic models studied over platinum catalysts, the Kahle-Deutschmann mechanism [24] was selected for further evaluation of experiments in this work due to being thermodynamically consistent, in contrast to the model by Quiceno et al. [19]. Thus, reversibility of forward and backward reactions is ensured microkinetically [42]. It is noteworthy that no catalytic coupling reactions are taken into consideration over the surface. The mechanisms are available electronically (Available online: www.detchem.com/mechanisms (accessed on May 6, 2021).

4. Conclusions

In this work, a combined experimental and simulation investigation on oxidative coupling of methane over Pt/Al_2O_3 was conducted employing detailed kinetic models from literature for both surface kinetics over Pt and gas phase kinetics. Varying the reaction conditions during experiments revealed that low N_2 dilution and higher space velocity favors the formation of C2 species. However, when increasing the GHSV beyond 4.5×10^5 h^{-1}, we found a decline in C2 selectivity. Experiments at different inlet CH_4/O_2 ratios showed a maximum C2 selectivity of 7% C2 with 94% CH_4 conversion at a CH_4/O_2 ratio of 2.

The simulation investigation of the oxidative coupling over Pt monoliths showed that both heterogeneous and homogeneous chemistry together are required for describing the formation of C2 species. The highly active Pt catalyst facilitates the exothermic oxidation of methane, consuming the majority of the oxygen on the catalyst surface and simultaneously increasing the temperature. The remaining oxygen and desorbed OH radicals facilitate the formation of CH_3 radicals from CH_4 in the gas-phase downstream of the monolith, which can then participate in coupling reactions to form C2 species. Among the C2 species, C_2H_2 is the main product. However, depending on the CH_4/O_2 ratio at the inlet and, consequently, at the outlet conditions of the monolith, the ratio of CO_2/CH_4 in the reaction gas stream plays a key role in the further consumption of C_2H_2 and can decrease the overall obtained selectivity of the process. Additionally, the simulation results do not agree completely with the experimental ones with respect to the distribution of C2 species but describe the total C2 selectivity well. These discrepancies are likely because the kinetic model was not initially developed for OCM and, thus, some gas phase reactions affecting the formation of C2 species require further tuning. Future studies

should, additionally, lay particular focus on considering interacting species and reactions combining the two mechanisms.

It is evident that in order to optimize the selectivity of the desired products, the reaction conditions and reactor parameters should be selected carefully. Understanding the impact of various reaction conditions on the product selectivity is significant for both academia and industry.

Appendix A

Figure A1. Reaction Flow Analysis of PolyMech Mechanism at 1673 K, CH_4/O_2 ratio = 1.4 (35% N_2, p = 1 bar), here * denotes the free radical species.
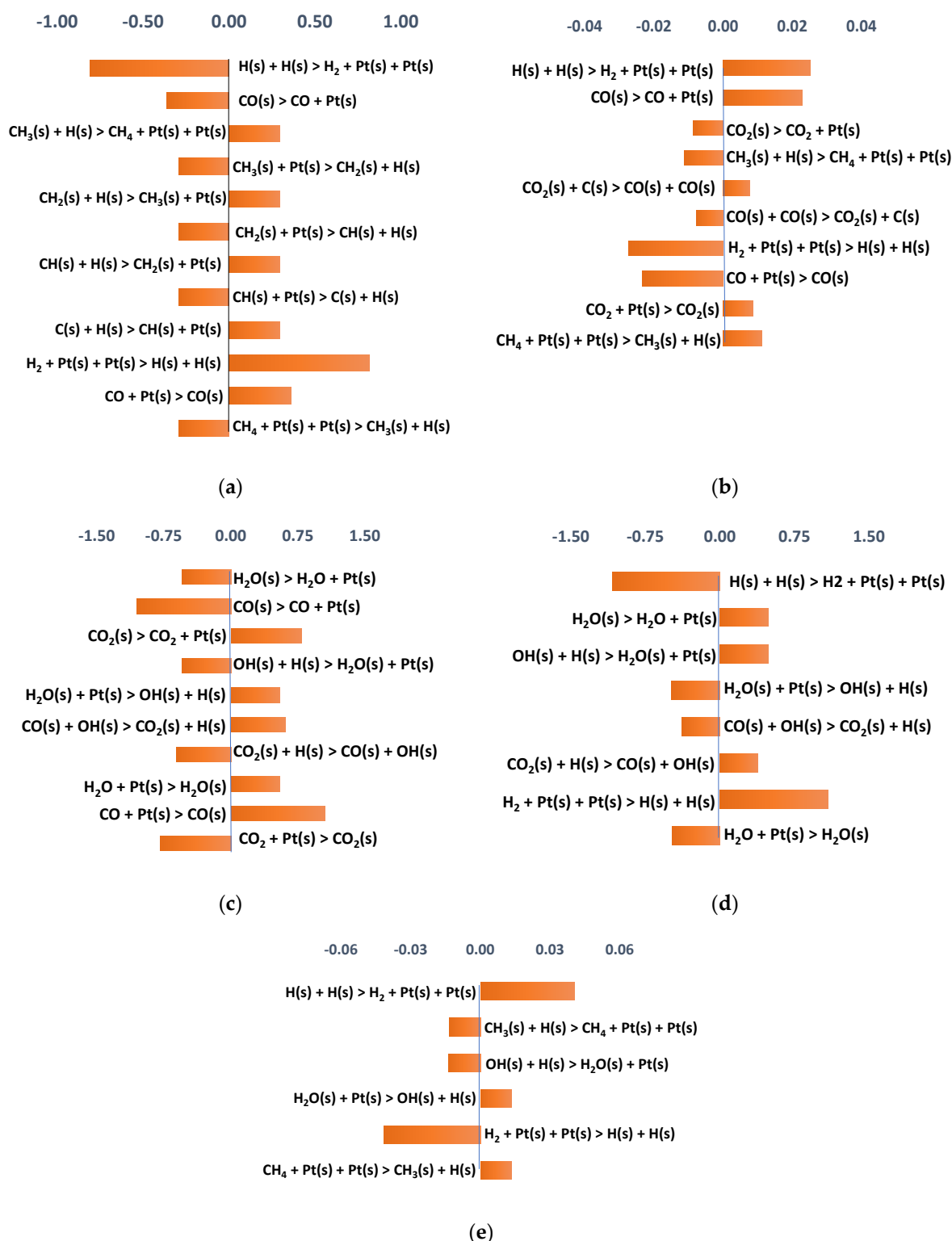
Figure A2. Sensitivity Analysis of Kahle-Deutschmann Mechanism at adiabatic conditions, T_{inlet} = 773 K, CH_4/O_2 ratio = 1.4 (35% N_2, p = 1 bar), normalized absolute sensitivity values for (**a**) CH_4 conversion; (**b**) H_2O formation; (**c**) CO_2 formation; (**d**) CO formation; (**e**) H_2 formation.

References

1. Horn, R.; Schlögl, R. Methane Activation by Heterogeneous Catalysis. *Catal. Lett.* **2015**, *145*, 23–39. https://doi.org/10.1007/s10562-014-1417-z.

2. Wang, B.; Albarracín-Suazo, S.; Pagán-Torres, Y.; Nikolla, E. Advances in methane conversion processes. *Catal. Today* **2017**, *285*, 147–158. https://doi.org/10.1016/j.cattod.2017.01.023.

3. Keller, G.E.; Bhasin, M.M. Synthesis of ethylene via oxidative coupling of methane. I. Determination of active catalysts. *J. Catal.* **1982**, *73*, 9–19. https://doi.org/10.1016/0021-9517(82)90075-6.

4. Yunarti, R.T.; Lee, M.; Hwang, Y.J.; Choi, J.W.; Suh, D.J.; Lee, J.; Kim, I.W.; Ha, J.M. Transition metal-doped TiO_2 nanowire catalysts for the oxidative coupling of methane. *Catal. Commun.* **2014**, *50*, 54–58. https://doi.org/10.1016/j.catcom.2014.02.026.

5. Galadima, A.; Muraza, O. Revisiting the oxidative coupling of methane to ethylene in the golden period of shale gas: A review. *J. Ind. Eng. Chem.* **2016**, *37*, 1–13.

6. Ghiasi, M.; Malekzadeh, A.; Hoseini, S.; Mortazavi, Y.; Khodadadi, A.; Talebizadeh, A. Kinetic study of oxidative coupling of methane over Mn and/or W promoted Na_2SO_4/SiO_2 catalysts. *J. Nat. Gas. Chem.* **2011**, *20*, 428–434. https://doi.org/10.1016/S1003-9953(10)60199-5.

7. Conway, S.J.; Wang, D.J.; Lunsford, J.H. Selective oxidation of methane and ethane over Li+-MgO-Cl- catalysts promoted with metal oxides. *Appl. Catal. A Gen.* **1991**, *79*, L1–L5. https://doi.org/10.1016/0926-860X(91)85001-E.

8. Spinicci, R.; Marini, P.; de Rossi, S.; Faticanti, M.; Porta, P. Oxidative coupling of methane on $LaAlO_3$ perovskites partially substituted with alkali or alkali-earth ions. *J. Mol. Catal. A Chem.* **2001**, *176*, 253–265. https://doi.org/10.1016/S1381-1169(01)00265-5.

9. Karakaya, C.; Zhu, H.; Zohour, B.; Senkan, S.; Kee, R.J. Detailed Reaction Mechanisms for the Oxidative Coupling of Methane over La_2O_3/CeO_2 Nanofiber Fabric Catalysts. *ChemCatChem* **2017**, *9*, 4538–4551. https://doi.org/10.1002/cctc.201701172.

10. Feng, Y.; Niiranen, J.; Gutman, D. Kinetic studies of the catalytic oxidation of methane. 2. Methyl radical recombination and ethane formation over 1% Sr/La_2O_3. *J. Phys. Chem.* **1991**, *95*, 6564–6568. https://doi.org/10.1021/j100170a036.

11. Trueba, M.; Trasatti, S.P. γ-alumina as a support for catalysts: A review of fundamental aspects. *Eur. J. Inorg. Chem.* **2005**, 3393–3403. https://doi.org/10.1002/ejic.200500348.

12. Chen, B.; Zhao, Q.; Yu, L.; Chen, L.; Crocker, M.; Shi, C. New insights into the size and support effects of γ-Al_2O_3 supported Au catalysts for HCHO oxidation at room temperature. *Catal. Sci. Technol.* **2020**, *10*, 4571–4579. https://doi.org/10.1039/d0cy00857e.

13. Korup, O.; Goldsmith, C.F.; Weinberg, G.; Geske, M.; Kandemir, T.; Schlögl, R.; Horn, R. Catalytic partial oxidation of methane on platinum investigated by spatial reactor profiles, spatially resolved spectroscopy, and microkinetic modeling. *J. Catal.* **2013**, *297*, 1–16. https://doi.org/10.1016/j.jcat.2012.08.022.

14. Hohn, K.L.; Witt, P.M.; Davis, M.B.; Schmidt, L.D. Methane coupling to acetylene over Pt-coated monoliths at millisecond contact times. *Catal. Lett.* **1998**, *54*, 113–118. https://doi.org/10.1023/A:1019092308769.

15. Thybaut, J.W.; Sun, J.; Olivier, L.; van Veen, A.C.; Mirodatos, C.; Marin, G.B. Catalyst design based on microkinetic models: Oxidative coupling of methane. *Catal. Today* **2011**, *159*, 29–36. https://doi.org/10.1016/j.cattod.2010.09.002.

16. Lunsford, J.H. The Catalytic Oxidative Coupling of Methane. *Angew. Chem. Int. Ed. Engl.* **1995**, *34*, 970–980. https://doi.org/10.1002/anie.199509701.

17. Grace, W.R.; Angeles, L. Kinetics of the Oxidative of Methane over 1 wt-% Sr/La_2O_3. *J. Catal.* **1988**, *118*, 517-524.

18. Labinger, J.A. Oxidative coupling of methane: An inherent limit to selectivity? *Catal. Lett.* **1988**, *1*, 371–375. https://doi.org/10.1007/BF00766166.

19. Quiceno, R.; Pérez-Ramírez, J.; Warnatz, J.; Deutschmann, O. Modeling the high-temperature catalytic partial oxidation of methane over platinum gauze: Detailed gas-phase and surface chemistries coupled with 3D flow field simulations. *Appl. Catal. A Gen.* **2006**, *303*, 166–176. https://doi.org/10.1016/j.apcata.2006.01.041.

20. Geske, M.; Pelzer, K.; Horn, R.; Jentoft, F.C.; Schlögl, R. In-situ investigation of gas phase radical chemistry in the catalytic partial oxidation of methane on Pt. *Catal. Today* **2009**, *142*, 61–69. https://doi.org/10.1016/j.cattod.2009.01.005.

21. Deutschmann, O.; Tischer, S.; Correa, C.; Chatterjee, D.; Kleditzsch, S.; Janardhanan, V.; Mladenov, N.; Minh, H.D.; Karadeniz, H.; Hettel, M.; Menon V., Banerjee V., Goßler H., Daymo, E. *DETCHEM Software package, 2.8 ed.*, Karlsruhe, Germany, 2020.

22. Schwiedernoch, R.; Tischer, S.; Correa, C.; Deutschmann, O. Experimental and numerical study on the transient behavior of partial oxidation of methane in a catalytic monolith. *Chem. Eng. Sci.* **2003**, *58*, 633–642. https://doi.org/10.1016/S0009-2509(02)00589-4.

23. Porras, S.; Kaczmarek, D.; Herzler, J.; Drost, S.; Werler, M.; Kasper, T.; Fikri, M.; Schießl, R.; Atakan, B.; Schulz, C.; et al. An experimental and modeling study on the reactivity of extremely fuel-rich methane/dimethyl ether mixtures. *Combust. Flame* **2020**, *212*, 107–122. https://doi.org/10.1016/j.combustflame.2019.09.036.

24. Kahle, L.C.S.; Roussière, T.; Maier, L.; Herrera Delgado, K.; Wasserschaff, G.; Schunk, S.A.; Deutschmann, O. Methane dry reforming at high temperature and elevated pressure: Impact of gas-phase reactions. *Ind. Eng. Chem. Res.* **2013**, *52*, 11920–11930. https://doi.org/10.1021/ie401048w.

25. Witt, P.M.; Schmidt, L.D. Effect of flow rate on the partial oxidation of methane and ethane. *J. Catal.* **1996**, *163*, 465–475. https://doi.org/10.1006/jcat.1996.0348.

26. Sarsani, S.; West, D.; Liang, W.; Balakotaiah, V. Autothermal oxidative coupling of methane with ambient feed temperature. *Chem. Eng. J.* **2017**, *328*, 484–496. https://doi.org/10.1016/j.cej.2017.07.002.

27. Kooh, A.; Dubois, J.L.; Mimoun, H.; Cameron, C.J. Oxidative coupling of methane: Maximizing the yield of coupling products under cofeed operating conditions. *Catal. Today* **1990**, *6*, 453–462. https://doi.org/10.1016/0920-5861(90)85039-Q.

28. Takanabe, K.; Iglesia, E. Mechanistic aspects and reaction pathways for oxidative coupling of methane on Mn/Na$_2$WO$_4$/SiO$_2$ catalysts. *J. Phys. Chem. C* **2009**, *113*, 10131–10145. https://doi.org/10.1021/jp9001302.

29. Stein, S.E.; Fahr, A. High-temperature stabilities of hydrocarbons. *J. Phys. Chem.* **1985**, *89*, 3714–3725. https://doi.org/10.1021/j100263a027.

30. Savchenko, V.I.; Zimin, Y.S.; Nikitin, A.V.; Sedov, I.V.; Arutyunov, V.S. Non-Catalytic Steam Reforming of C1–C4 Hydrocarbons. *Pet. Chem.* **2021**, *61*, 762–772. https://doi.org/10.1134/S0965544121070021.

31. Buras, Z.J.; Safta, C.; Zádor, J.; Sheps, L. Simulated production of OH, HO$_2$, CH$_2$O, and CO$_2$ during dilute fuel oxidation can predict 1st-stage ignition delays. *Combust. Flame* **2020**, *216*, 472–484. https://doi.org/10.1016/j.combustflame.2019.12.013.

32. Savchenko, V.I.; Nikitin, A.V.; Sedov, I.V.; Ozerskii, A.V.; Arutyunov, V.S. The role of homogeneous steam reforming of acetylene in the partial oxidation of methane to syngas in matrix type converters. *Chem. Eng. Sci.* **2019**, *207*, 744–751. https://doi.org/10.1016/j.ces.2019.07.012.

33. Zhu, J.; Zhang, D.; King, K.D. Reforming of CH$_4$ by partial oxidation: Thermodynamic and kinetic analyses. *Fuel* **2001**, *80*, 899–905. https://doi.org/10.1016/S0016-2361(00)00165-4.

34. Hiblot, H.; Ziegler-Devin, I.; Fournet, R.; Glaude, P.A. Steam reforming of methane in a synthesis gas from biomass gasification. *Int. J. Hydrog. Energy* **2016**, *41*, 18329–18338. https://doi.org/10.1016/j.ijhydene.2016.07.226.

35. Angeli, S.D.; Gossler, S.; Lichtenberg, S.; Kass, G.; Agrawal, A.K.; Valerius, M.; Kinzel, K.P.; Deutschmann, O. Reduction of CO$_2$ Emission from Off-Gases of Steel Industry by Dry Reforming of Methane. *Angew. Chem. Int. Ed.* **2021**, *60*, 11852–11857. https://doi.org/10.1002/anie.202100577.

36. Savchenko, V.I.; Zimin, Y.S.; Nikitin, A.V.; Sedov, I.V.; Arutyunov, V.S. Utilization of CO$_2$ in non-catalytic dry reforming of C1-C4hydrocarbons. *J. CO2 Util.* **2021**, *47*, 101490. https://doi.org/10.1016/j.jcou.2021.101490.

37. Gänzler, A.M.; Casapu, M.; Doronkin, D.E.; Maurer, F.; Lott, P.; Glatzel, P.; Votsmeier, M.; Deutschmann, O.; Grunwaldt, J.-D. Unravelling the Different Reaction Pathways for Low Temperature CO Oxidation on Pt/CeO$_2$ and Pt/Al$_2$O$_3$ by Spatially Resolved Structure-Activity Correlations. *J. Phys. Chem. Lett.* **2019**, *10*, 7698–7705. https://doi.org/10.1021/acs.jpclett.9b02768.

38. Karinshak, K.A.; Lott, P.; Harold, M.P.; Deutschmann, O. In situ Activation of Bimetallic Pd–Pt Methane Oxidation Catalysts. *ChemCatChem* **2020**, *12*, 3712–3720. https://doi.org/10.1002/cctc.202000603.

39. Chan, D.; Tischer, S.; Heck, J.; Diehm, C.; Deutschmann, O. Correlation between catalytic activity and catalytic surface area of a Pt/Al$_2$O$_3$ DOC: An experimental and microkinetic modeling study. *Appl. Catal. B Environ.* **2014**, *156–157*, 153–165. https://doi.org/10.1016/j.apcatb.2014.03.009.

40. Bruix, A.; Margraf, J.T.; Andersen, M.; Reuter, K. First-principles-based multiscale modelling of heterogeneous catalysis. *Nat. Catal.* **2019**, *2*, 659–670. https://doi.org/10.1038/s41929-019-0298-3.

41. Gossler, H.; Deutschmann, O. Numerical optimization and reaction flow analysis of syngas production via partial oxidation of natural gas in internal combustion engines. *Int. J. Hydrog. Energy* **2015**, *40*, 11046–11058. https://doi.org/10.1016/j.ijhydene.2015.06.125.

42. Herrera Delgado, K.; Maier, L.; Tischer, S.; Zellner, A.; Stotz, H.; Deutschmann, O. Surface reaction kinetics of steam- and CO$_2$-reforming as well as oxidation of methane over nickel-based catalysts. *Catalysts* **2015**, *5*, 871–904. https://doi.org/10.3390/catal5020871.

43. Gardiner, W.; Lissianski, V.; Qin, Z.; Smith, G.; Golden, D.; Frenklach, M.; Eiteneer, B.; Goldenberg, M.; Moriarty, N.; Bowman, C.; et al. The GRI-Mech(TM) Model for Natural Gas Combustion and NO Formation and Removal Chemistry. In Proceedings of the Fifth International Conference on Technologies and Combustion for a Clean Environment. 12–15 July 1999, 153–155.

44. Healy, D.; Curran, H.J.; Dooley, S.; Simmie, J.M.; Kalitan, D.M.; Petersen, D.K.; Bourque, G. Methane/propane mixture oxidation at high pressures and at high, intermediate and low temperatures. *Combust. Flame* **2008**, *155*, 451–461. https://doi.org/10.1016/j.combustflame.2008.06.008.

45. Naik, C.V.; Dean, A.M. Detailed kinetic modeling of ethane oxidation. *Combust. Flame* **2006**, *145*, 16–37. https://doi.org/10.1016/j.combustflame.2005.12.006.